

# Investigating short-time-scale variations in cometary ions around comet 67P

Gabriella Stenberg Wieser,<sup>1</sup>★ Elias Odelstad,<sup>2</sup> Martin Wieser,<sup>1</sup> Hans Nilsson,<sup>1</sup> Charlotte Goetz,<sup>3</sup> Tomas Karlsson,<sup>4</sup> Mats André,<sup>2</sup> Leif Kalla,<sup>1</sup> Anders I. Eriksson,<sup>2</sup> Georgios Nicolaou,<sup>1</sup> Cyril Simon Wedlund,<sup>5</sup> Ingo Richter<sup>3</sup> and Herbert Gunell<sup>6,7</sup>

<sup>1</sup>Swedish Institute of Space Physics, Box 812, SE-981 28 Kiruna, Sweden

<sup>2</sup>Swedish Institute of Space Physics, Box 537, SE-751 21 Uppsala, Sweden

<sup>3</sup>Institute for Geophysics and Extraterrestrial Physics, TU Braunschweig, D-38106 Braunschweig, Germany

<sup>4</sup>Department of Space and Plasma Physics, School of Electrical Engineering, KTH Royal Institute of Technology, Stockholm, Sweden

<sup>5</sup>Department of Physics, University of Oslo, P.O. box 1048, Blindern, N-0316 Oslo, Norway

<sup>6</sup>Royal Belgian Institute for Space Aeronomy, Avenue Circulaire 3, B-1180 Brussels, Belgium

<sup>7</sup>Department of Physics, Umeå University, SE-901 87 Umeå, Sweden

Accepted 2017 August 14. Received 2017 August 11; in original form 2017 April 4

## ABSTRACT

The highly varying plasma environment around comet 67P/Churyumov–Gerasimenko inspired an upgrade of the ion mass spectrometer (Rosetta Plasma Consortium Ion Composition Analyzer) with new operation modes, to enable high time resolution measurements of cometary ions. Two modes were implemented, one having a 4 s time resolution in the energy range 0.3–82 eV/q and the other featuring a 1 s time resolution in the energy range 13–50 eV/q. Comparing measurements made with the two modes, it was concluded that 4 s time resolution is enough to capture most of the fast changes of the cometary ion environment. The 1462 h of observations done with the 4 s mode were divided into hour-long sequences. It is possible to sort 84 per cent of these sequences into one of five categories, depending on their appearance in an energy–time spectrogram. The ion environment is generally highly dynamic, and variations in ion fluxes and energies are seen on time-scales of 10 s to several minutes.

**Key words:** plasmas – instrumentation: detectors – methods: data analysis – methods: statistical – space vehicles: instruments – comets: individual: 67P.

## 1 INTRODUCTION

Comets in the inner Solar system are highly variable and dynamic objects. As they approach the Sun, sublimation of the surface and subsurface material creates expanding atmospheres and long cometary tails. Long before space missions were possible, the naked eye could observe cometary tails, changing from day to day as a comet continued its journey around the Sun. Telescopic observations revealed that rapid dramatic processes may occur: a cometary tail may suddenly be discarded and reformed afterwards (Barnard 1920). Such phenomena became easier to interpret when it was proposed, and later discovered, that a flow of charged particles from the Sun (the solar wind) is constantly interacting with the comets (Biermann 1951; Alfvén 1957).

Cometary science made a huge step forward with the first spacecraft fly-bys of comets 21P/Giacobini–Zinner and 1P/Halley in 1985 and 1986. Flying in formation with a comet, the *Rosetta* mission (Glassmeier et al. 2007a) to 67P/Churyumov–Gerasimenko

(67P) gave us a unique possibility to study the interaction of the solar wind with a cometary atmosphere over a long time and in great detail. The highly dynamic plasma processes suggested by the observed fine-structured cometary tails and disconnecting tail events (Mendis & Ip 1977) could now be investigated with the plasma instruments *in situ* by the Rosetta Plasma Consortium (RPC; Carr et al. 2007).

The near comet space of 67P truly offers a complex environment. A rotating irregularly shaped comet nucleus with constantly changing illumination conditions (Sierks et al. 2015) leads to variations in outgassing (Bieler et al. 2015), and dust grains, originating from the surface, mixing with the released neutral gas. The neutral gas streaming away from the nucleus is partially ionized by solar ultraviolet radiation (EUV), charge-exchange reactions and electron ionization (Cravens et al. 1987). Newly born ions, still coupled to the neutrals via collisions in the inner coma, then start interacting with the solar wind. As long as the neutral gas is thin enough, the solar wind permeates the comet’s atmosphere, but when the outgassing increases as the comet moves closer to the Sun, more or less stable plasma boundaries form: a cometary magnetosphere, similar to what is observed around

\* E-mail: [gabriella@irf.se](mailto:gabriella@irf.se)

unmagnetized planets, is created (Cravens & Gombosi 2004; Nilsson et al. 2015). The mass spectrometer, Rosetta Plasma Consortium Ion Composition Analyzer (RPC-ICA; Nilsson et al. 2007), continuously observed solar wind ions when the comet was at heliocentric distances larger than about 1.7 au (Behar et al. 2017). Between 2015 April 28 and December 11, only sporadic observations of solar wind ions were made and the *Rosetta* spacecraft was located inside a solar wind cavity. The diamagnetic cavity, the magnetic field-free region surrounding the nucleus, was probed at multiple occasions between 2015 April 20 and 2016 February 17 (Goetz et al. 2016b).

It is not surprising that short-time-scale, spatially fine-structured and transient plasma phenomena are to be found in such complex and dynamic environment. The question is rather which temporal and spatial scales are dominant and characteristic of different plasma regions around 67P during different time periods in the evolution of the cometary magnetosphere.

A fundamental time-scale governing the comet environment is the orbital period of 6.5 yr. The neutral outgassing rate changes in response to the heliocentric distance (Hansen et al. 2016). On shorter time-scales, the comet's rotation period of 12.4 h (Sierks et al. 2015) manifests itself as a variation of 6.2 h in the observed neutral density (Hässig et al. 2015) as well as in the ion and electron density (Edberg et al. 2015). The illuminated neck region between the two lobes acted as a strong source of neutrals at the time *Rosetta* arrived at 67P.

One of the earliest observed signatures of a faster varying plasma environment was a strong modulation of the magnetic field at a frequency around 40 mHz known as 'the singing comet' (Richter et al. 2015). Currents composed of newborn cometary ions are suggested responsible for the growth of these large-amplitude compressional magnetic field oscillations (Meier, Glassmeier & Motschmann 2016). On even smaller scales, electric field measurements show the presence of waves close to the  $\text{H}_2\text{O}^+$  lower hybrid frequency with amplitudes of  $\sim 50 \text{ mV m}^{-1}$ . The largest amplitudes are observed on steep density gradients (Karlsson et al. 2017). Assuming that the density gradient convects over the spacecraft with a typical velocity of the neutral gas ( $0.7 \text{ km s}^{-1}$ ), the scale size of a gradient is estimated to be 13 km.

Hybrid simulations also suggest a large degree of spatial structure and temporal evolution in the plasma density around comet 67P (Koenders et al. 2015). For example, plasma density and magnetic field strength are predicted to change on a time-scale of a few seconds (Koenders et al. 2015, figs 3c and d).

*Rosetta* was moving around comet 67P with a walking pace, which should enable very high spatial resolution also with modest temporal resolution if the observed environment is reasonable stable. This paper focuses on rapid changes in the ion environment around comet 67P as detected by the RPC-ICA (Nilsson et al. 2007) on board the *Rosetta* spacecraft. We will first describe how the time resolution was increased and two new observation modes introduced. These modes enabled measurements of cometary ions with a temporal resolution of 4 or 1 s in limited energy ranges and were not planned prior to the arrival at the comet in 2014 August. We will then analyse the recorded high time resolution data with the focus on identifying typical time-scales.

## 2 INSTRUMENTATION

The ion observations analysed in this paper are made by the RPC-ICA (Nilsson et al. 2007). RPC-ICA observes direction of arrival, energy per charge and mass per charge of ions around 67P, and

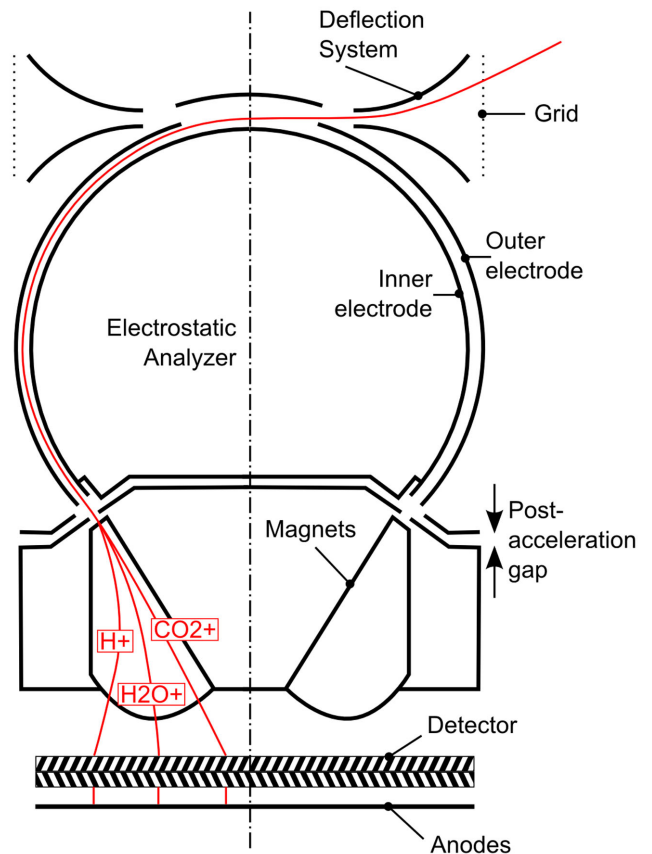


**Figure 1.** Cross-section of RPC-ICA. The deflection system, the ESA, the magnetic momentum filter and the detector plate are indicated. The instrument is cylindrically symmetric around the dash-dotted line and hence covers all azimuthal angles.

the instrument and its high time resolution observation modes are described in detail in the following subsections. To better interpret the ion measurements, we use data from the Langmuir probes (RPC-LAP; Eriksson et al. 2007) and the magnetometer (RPC-MAG; Glassmeier et al. 2007b) on *Rosetta*. These sensors are also presented below.

### 2.1 The ion composition analyzer

The ion mass spectrometer RPC-ICA consists of four cylindrically symmetric parts. These are an entrance deflection system, an electrostatic analyzer (ESA), a magnetic momentum filter and a detector plate. The aperture is  $360^\circ \times 5^\circ$  in the plane perpendicular to the symmetry axis. A schematic sketch of the instrument is presented in Fig. 1.

The entrance deflection system consists of two plates. By changing the electrostatic potential of the two plates, ions from directions out of the aperture plane can enter the instrument. For ion energies above  $105 \text{ eV/q}$  and below  $14 \text{ keV/q}$ , the instrument is able to scan directions  $\pm 45^\circ$  (elevation angles) with respect to the aperture plane. We use 16 different elevation angles, which, for telemetry reasons, are sometimes binned together before transmission to ground.

For ion energies below  $105 \text{ eV/q}$ , the required potential changes on the deflection plates are too small compared to the available resolution of the internal digital-to-analogue converters. In this energy range, we are still stepping the deflection voltages in order to be certain not to miss the signal entirely, but the most of the ions

we detect are arriving from a direction close to the aperture plane. The field of view is almost two-dimensional,  $5 \times 360^\circ$ . Similarly, at high ion energies above 14 keV/q, the required voltage on the deflection plates to reach  $\pm 45^\circ$  out of the aperture plane exceeds the capabilities of the high-voltage power supplies. The available elevation range is then limited to less than  $\pm 45^\circ$ .

The entrance system is covered by a conductive grid that could be put to a negative voltage of 12 V relative to the spacecraft to repel thermal electrons and attract thermal ions. However, during most of *Rosetta*'s 2 yr mission, the spacecraft was negatively charged and the grid was grounded to the spacecraft potential at all times.

After entering RPC-ICA through the deflection system, positive ions reach the spherical ESA. The ESA is designed to cover an energy range of 5–40 keV/q with an energy resolution of  $dE/E = 0.07$ . At very low energies ( $< 30$  eV), the effective energy resolution of the instrument changes up to  $dE/E = 0.30$  due to pre-acceleration of particles into the ESA. The ESA consists of two hemispherical electrodes separated by a gap of 2.2 mm width. The centre line of the gap has a radius of 45.0 mm. Setting different voltages on the electrodes creates an electric field between them, and if the energy per charge of the incoming ion matches the electric field, the ion passes through the ESA and continues into the magnetic momentum section of the instrument. Nominally, RPC-ICA uses 96 energy steps to cover the whole energy range, and each energy sweep takes 12 s.

For ion energies above 97 eV/q, the outer electrode is kept at fixed low voltage (between 0 and 10 V), while the voltage of the inner electrode is changed in steps between 0 V and about 4 kV. For energies below 97 eV/q, the voltage of the outer electrode is changed with high resolution in the range 0–10 V, while the inner is kept fixed close to 0 V. The switch between stepping the voltage on the inner and outer electrode at 97 eV/q is made to provide an energy range from 5 to 40 keV/q, while keeping the resolution requirements for the internal digital-to-analogue converters that control the high-voltage supplies reasonable. Note that the high-voltage settings for elevation and energy are coupled. The deflection voltages needed to reach a certain arrival direction of ions are energy dependent.

The third part of RPC-ICA contains 16 magnets giving rise to a circular magnetic field inside the cylindrical instrument. Depending on their momentum per charge, their trajectories will bend differently in the field. Ions with a larger momentum travel along a straighter trajectory. Since the energy per charge of the ions entering the magnetic section for a given energy step is the same, heavy ions will hit the circular detector plate at the bottom of the sensor close to the centre. The trajectories of lighter ions are more affected by the magnetic field and these ions hit the detector at a larger distance from the centre. The impact position on the detector of an ion with a certain energy and mass per charge is calibrated on ground before launch. The entire magnet assembly can be put on high voltage resulting in a post-acceleration of ions leaving the ESA, prior entering the circular magnetic field. This results in a shift of the impact position on the detector. By selecting the post-acceleration potential, the mass per charge of an ion impacting on a certain position can be adjusted in flight and focus can be given e.g. to light or heavy ions.

A micro-channel plate (MCP) is used as a detector. The impact position of a particle is determined by a set of discrete charge collecting anodes on the exit side of the MCP. There are 32 ring-shaped anodes that collect part of the electron cloud exiting the MCP. These ring-shaped anodes are used to measure the distance of the impact position from the centre. The other part of the electron cloud hits one of the 16 sector anodes used to measure arrival direction in azimuth direction. Signals from all 32 + 16 anodes are then

amplified and converted to digital signals for further processing. A successful particle detection consists of a simultaneous signal from one of the 32 mass rings and from one of the 16 sectors.

For each elevation angle, an energy sweep covering 96 energy steps is made before changing to the next elevation angle. In total, 16 elevations are scanned and since each energy sweep takes 12 s, the nominal time resolution of RPC-ICA is  $16 \times 12 = 192$  s. All azimuthal arrival directions and all mass rings are measured simultaneously.

### 2.1.1 The RPC-ICA energy offset

When arriving at comet 67P, it was discovered that the high voltage controlling the inner ESA electrode had an offset of more than 33 V as compared to laboratory calibration results. Using housekeeping data and ion measurements obtained while at the comet, the offset voltage could be determined to within a level of about 1 V, leaving an uncertainty of the exact energy level of the detected ions of about 10 eV/q. Data corrected to this level were used to do the original categorization of the data into the types shown in Section 4.2.

Some case studies indicated that the energy levels estimated in this way are about 10 eV/q too high (Gunell et al. 2017). Comparison with spacecraft potential estimates from the RPC-LAP Langmuir probe confirmed this and allowed us to further improve the correction (Odelstad et al. 2017): an additional offset of  $-13.7$  eV/q applied to the energy scale resulted in a remaining uncertainty of the current best energy level estimate of about 2 eV/q. Unless mentioned otherwise, all energy ranges and all data shown in this paper are reprocessed and corrected to this more accurate energy scale. The energy table in Appendix A is also corrected for this offset.

Apart from the remaining uncertainty, there is a temperature-related drift of the related high voltage, which affects measurements at instrument temperatures below  $13.5^\circ\text{C}$ . However, all the example cases shown in this study were obtained with instrument temperatures above  $13.5^\circ\text{C}$ .

## 2.2 Implementation of high time resolution modes

As described above, RPC-ICA was not designed for high time resolution measurements. However, arriving at comet 67P and looking at the first observations of cometary ions (Nilsson et al. 2015), we realized that ion environment was highly variable. Observations from other instruments on board *Rosetta* confirmed this picture (see Section 1).

### 2.2.1 4 s time resolution

Considering that the cometary ions are often observed within a limited energy range (20–100 eV/q), we can make a faster energy sweep by reducing the number of energy steps. However, the onboard software supports lookup tables for 96 energy steps, and to update and validate the software in-flight would be very complicated and risky. Still, we can achieve our goal by updating only the lookup tables, which is an acceptable minimal change. Instead of putting 96 different reference values that are translated to 96 different settings of the ESA electrode voltages, we specify only 32 different reference values but repeat them three times. The instrument observation cycle is exactly as before, but the time needed for an energy sweep is reduced to 4 s. A complication is that for each complete 96-step-long energy sweep, the onboard software allows maximum one switch between stepping the voltage of the outer and the inner electrode. To

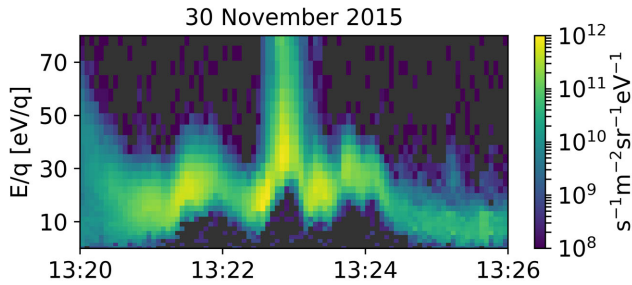


**Figure 2.** Energy–time spectrogram with 4 s time resolution.

get the same 32 energy settings repeated three times, all 32 energy steps must be either completely above or below 97 eV/q, where the switching would occur. The nominal energy range selected was 5–95 eV/q, to cover the low-energy cometary ion population that is most dynamic and most often seen (Nilsson et al. 2017). Due to the energy offset correction, this resulted finally in an usable energy range of 0.3–82 eV/q. As precise elevation scanning is not possible below 105 eV/q and as elevation scanning cannot be combined in a useful way with the three repeated energy sweeps, the elevation reference is put to the same value for all 16 elevation steps in the lookup table. The resulting elevation angle in this case is close to  $0^\circ$  and almost independent of energy. Hence, we get an observation mode with an energy range of 0.3–82 eV/q, a field of view of  $5 \times 360^\circ$  and a time resolution of 4 s. An example of data acquired using this mode is shown in Fig. 2.

The energy steps in this 4 s mode were selected to achieve a dense energy coverage, that is, no gaps between different energy bins. This is an additional advantage compared to the normal 96-step energy sweep, where there are gaps in the energy coverage at the lowest energies (below 80 eV/q). The implementation of a high time resolution mode in the way described was possible as the energy sweep was the inner faster loop and the elevation sweep the slower outer loop in the sweeping scheme. For the instrument to really produce the desired 4 s resolution, we also had to assure that elevation binning is prohibited. The instrument automatically reduces the produced data volume if a certain limit is exceeded. Reducing data volume is done by adding neighbouring azimuth or elevation angles, or by adding signals from neighbouring mass rings together. In the new mode, however, the high time resolution would be lost if different elevations would be combined. The first attempt to use this observation mode was done on 2015 April 28, but that run suffered from the elevation binning problem as did many of the observations recorded in 2015 May. The last use of the 4 s mode was on the 23rd of September 2016, a week before the end of mission. In total, 1462 h of data using the 4 s mode were recorded during the mission, with 1358 h of the data set correctly binned.

### 2.2.2 1 s time resolution

In addition, an even faster mode was created. With only eight energy steps covering the range 13–50 eV/q, the time resolution was brought down to 1 s (Fig. 3a). This mode does not provide a dense coverage of the energy range and the risks are higher that a considerable part of the low-energy ion population we want to capture moves out of the covered energy interval. This mode also shows the tendency of resulting in data gaps due to overproduction of data. Such overproduction happens because of the prohibited elevation binning (see Section 2.2.1) that prevents one of the data volume reduction mechanisms from working and because of the lower ef-

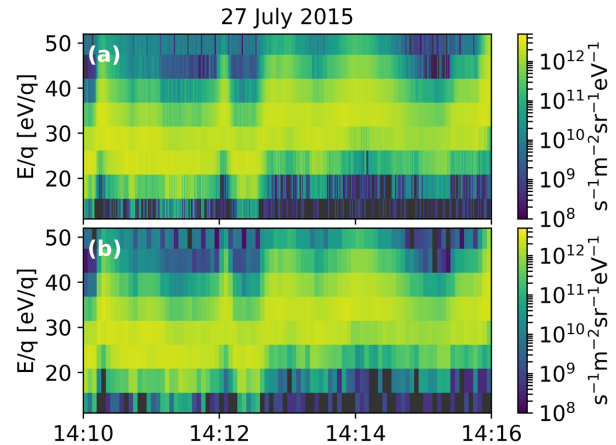


**Figure 3.** (a) Energy–time spectrogram with 1 s time resolution. (b) The same data as in panel (a) but resampled to 4 s resolution.

iciency of the data compression as the data in this mode contain a rather large fraction of non-zero elements. For these reasons and the additional arguments put forward in Section 3.1, this faster mode was run only for rather limited times. In total, there are almost 49 h of data recorded using this observation mode from 2015 April 28 until 2015 August 3. During 48 of the 49 h recorded, no elevation steps were automatically added together during the observation. Hence, the data do not suffer from the binning problem described in the previous section and the time resolution is truly 1 s.

### 2.2.3 125 ms time resolution

Already from the start, there was the possibility to run RPC-ICA with both energy and elevation sweeping turned off. Operating the instrument this way results in a time series with a time resolution of 125 ms (basically the acquisition time) containing the ion counts at one fixed energy. This possibility was assumed to be of limited scientific interest and was used only once during the entire mission. The necessary command was executed on 2015 August 13, and just over 3 h of data were obtained.

## 2.3 The Langmuir probes

The Rosetta Langmuir Probe instrument (RPC-LAP) consists of two spherical Langmuir probes, LAP1 and LAP2, of 2.5 cm radii, located at the ends of two booms of lengths 2.2 and 1.6 m, respectively, mounted on the spacecraft main body (RPC-LAP; Eriksson et al. 2007). Langmuir probes in general, and RPC-LAP in particular, are versatile instruments that can employ a number of different measurement techniques to measure an assortment of plasma parameters, e.g. electron and ion densities and temperatures, spacecraft potential, UV flux (Johansson et al. 2017) and mean ion mass. The availability of reliable measurements of any or all of these parameters depends on the specific instrument design, the ambient plasma environment, including possible spacecraft perturbations, the availability of extraneous measurements for cross-calibration and the specific measurement mode run by the instrument during any interval of interest. In the present study, we use measurements of the spacecraft potential ( $V_{S/C}$ ) obtained by LAP1 during the periods when RPC-ICA was run in the aforementioned high time resolution mode.

RPC-LAP has two different measurement modes capable of providing measurements of the spacecraft potential: (1) Langmuir probe sweeps and (2) electric field mode with floating probes (or a non-zero bias current, not used in the part of the mission studied here). In a Langmuir probe sweep (1), a bias potential is applied to the probe and then sequentially stepped through a potential range at most from  $-31$  to  $+31$  V with respect to the spacecraft. At least one of the LAP probes is sunlit at any given time, and this one can be used to find an estimate  $V_{\text{ph}}$  of the spacecraft potential by identification of the ‘photoelectron knee’, i.e. the limiting bias voltage for saturation of the photoelectron emission current (Odelstad et al. 2015; Eriksson et al. 2017).

Due to the boom lengths being shorter than, or comparable to, typical Debye lengths in the cometary plasma (Edberg et al. 2015; Galand et al. 2016), the local plasma potential at the location of the probe is generally somewhat negative with respect to the plasma at infinity, due to the influence of the negatively charged spacecraft. Therefore, the above method only picks up some fraction  $\alpha$ , typically of the order of 0.7–1 (Odelstad et al. 2017), of the full spacecraft potential  $V_{\text{S/C}}$ . A correction factor  $1/\alpha$  therefore needs to be applied to  $V_{\text{ph}}$  in order to obtain  $V_{\text{S/C}}$ . Langmuir probe sweeps are performed on any one probe with a cadence not larger than 32 s.

RPC-LAP is intermittently run with floating probes (2), i.e. with the probes disconnected from the biasing circuitry, sampling the probe potentials at high time resolution ( $\sim 60$  Hz). This is the standard way of measuring electric fields in a dense plasma (Maynard 1998) and has proven fruitful for electric field measurements at 67P (Karlsson et al. 2017). An estimate of the spacecraft potential can also be obtained from this measurement mode, since a floating probe will be at a potential  $V_{\text{F}}$  generally only a few volts from that of the local plasma potential. Reversing the sign of the measured probe-to-spacecraft potential  $V_{\text{F}} - V_{\text{S/C}}$  thus yields essentially the same estimate of  $V_{\text{S/C}}$  as that obtained from the sweeps above, with the addition of a generally unknown offset of the order of a few volts. A more detailed analysis of RPC-LAP spacecraft potential measurements, including a cross-calibration with RPC-ICA for constraining the fraction  $\alpha$  above, is provided in a companion paper (Odelstad et al. 2017).

In this paper, we use the spacecraft potential estimates resulting from floating probes to be able to compare fast variations in the ions with equally fast changes of  $V_{\text{S/C}}$ . We note that spacecraft potential is only known to a certain accuracy, which is not a limitation here as we are mostly interested in variations of the potential on time-scales of tens of seconds. We also present the electric field obtained at the same occasions.

## 2.4 The magnetometer

The magnetometer RPC-MAG (Glassmeier et al. 2007b) was designed to measure the magnetic field in a range of  $\pm 16384$  nT with a resolution of 31 pT. In the time domain, the magnetometer samples 20 vectors per second, i.e. with a sampling frequency of 20 Hz. Although the magnetometer consists of two individual units mounted on a boom, we only use measurements from the outboard magnetometer (RPC-MAG-OB) as it is located further away from the spacecraft and is therefore less influenced by artificial spacecraft fields than the second unit.

Although the location minimizes the unwanted field contributions, there still remain several unwanted signatures in the measurements. A prominent example is the spacecraft reaction wheels, used to keep position, which generate high-frequency, time-dependent artificial fields that are picked up by the magnetometer. For that

reason, we only use data resampled to 1 Hz, as the reaction wheel frequencies are always above that. Although a temperature calibration of the sensor was performed before launch, it was found that a significant temperature dependence of the magnetometer offset remained. Fortunately, with the detection of a diamagnetic cavity at comet 67P, this offset could be determined and removed, leaving uncertainties in the magnetic field magnitude of a few nanotesla (Goetz et al. 2016b). These are due to yet uncorrected spacecraft fields.

## 3 COMPARISON BETWEEN DIFFERENT HIGH TIME RESOLUTION MODES

### 3.1 Is 4 s time resolution appropriate?

The choice of a 4 s mode for RPC-ICA is somewhat arbitrary. From the example energy–time spectrum shown in Fig. 2, we immediately note substantial variation both in flux, average energy and width of the energy distribution within a time-scale of a minute. Compared to the nominal time resolution of more than 3 min (192 s), the 4 s mode definitely gives new insights into cometary ion dynamics at shorter time-scales. The changes in Fig. 2 appear smooth suggesting that our time resolution is high enough to capture the relevant variations.

To further advocate the decision to prioritize the 4 s mode, we look at the observations made with the 1 s mode. Fig. 3(a) shows an example of such an observation. In this case, we capture the entire energy width of the ion population, but the coarse energy resolution is clearly visible and gives a blurred impression compared to Fig. 2. This is the prize we pay for increasing the time resolution.

The important question to address is: do we gain anything by increasing the time resolution? Fig. 3(b) shows how the data displayed in Fig. 3(a) would look like if it would have been sampled using a 4 s resolution. We note that obvious fast variations, such as the rapid change in energy occurring at 14:12 UT, are seen also with slightly slower sampling. At least from a visible inspection, there are no major apparent rapid changes captured with the 1 s mode [in panel (a)] but not with the 4 s mode [in panel (b)]. This, together with the very limited energy range and the data gap issue discussed in Section 2.2.2, is the base of our decision to mainly use the 4 s mode.

There are, however, variations on a faster time-scale than 4 s seen in the 1 s data. These signatures will be discussed in the next subsection.

### 3.2 Features of the 125 ms mode

Fig. 4 shows a 40-min-long time interval from 2015 August 13, when both elevation and energy sweeping were turned off. The black curve in the beginning of the interval shows the counts detected by the 4 s mode in the energy bin corresponding to 21 eV/q, just before turning energy sweeping off. The red curve displays the counts detected in the 125 ms mode, using a fixed energy of 21 eV/q. At first glance, the general behaviour is the same; since the energy of the observed ions varies, the signal at a fixed energy will vary in accordance. Zooming in [panel (b)], however, reveals rapid changes of the signal on the time-scale of about 2 s. The appearance is clearly artificial, and we believe it is caused by interference from the spacecraft systems or any of the other operating instruments but we have not yet identified the source. As the frequency is just below 0.5 Hz, it should be seen in 1 s data, and in fact the same frequency is observable in all of the 1 s sequences recorded during the summer of 2015. It is not seen in all energy bins, but normally in

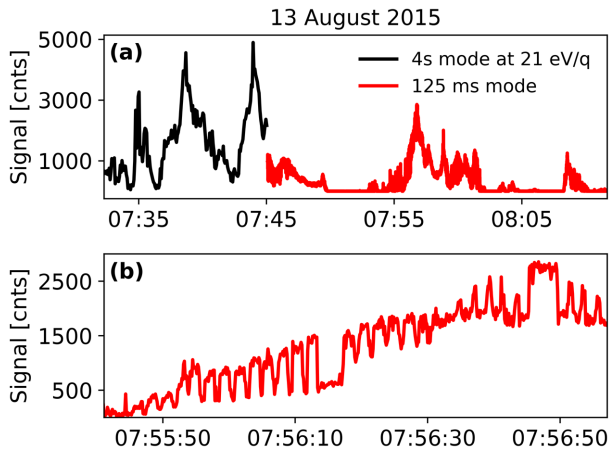


**Figure 4.** (a) The black curve shows the time series of the counts detected by the 4 s mode in one energy bin. The red curve shows the counts detected when elevation and energy sweeping were turned off and the energy fixed to 21 eV/q. (b) A shorter time interval of the 125 ms mode reveals artificial-looking time variations with a frequency of just below 0.5 Hz.

the lowest energy bin that contains a substantial number of counts. The frequency of the signal is always the same and the fact that the frequency stays constant over several months strengthens our hypothesis that the signal is spacecraft generated.

#### 4 CHARACTERIZING THE ION ENVIRONMENT AROUND 67P

After justifying the 4 s mode, we will now proceed to look at the data recorded with this observation mode during the mission. Our purpose is to give an overview of the measurements by sorting them into different types based on their appearance in an energy–time spectrogram. We will first describe how the sorting was done and what are the defining characteristics of each type. We then look at when and where the different types are observed before presenting them one by one. We are especially interested in any dominating time-scales. The ion observations are put in relation to simultaneous measurements of the spacecraft potential (observed by RPC-LAP), the magnetic field (from RPC-MAG) and the electric field fluctuations (detected by RPC-LAP).

##### 4.1 Data processing

To categorize the high time resolution observations, we first divided all data into hour-long observation sequences. This division was done automatically. A new sequence was started every time the 4 s mode was turned on. All the data recorded within the following hour were part of the same sequence even if there were data gaps. Depending on how long the 4 s mode was operated, additional hour-long sequences were defined.

Each sequence was displayed as an energy–time spectrogram. An example is given in Fig. 5. In total, 1462 h were recorded, but unfortunately the first attempts to use this observation mode suffered from binning in elevation, which ruined the time resolution during about 100 h, as described in Section 2.2.1.

The sequences with elevation binning were removed from further study. An additional number of sequences were removed from the current study for other reasons. The automatic division into hourly segments sometimes leads to sequences with a very limited amount of data. Therefore, all sequences containing less than 10 min of data

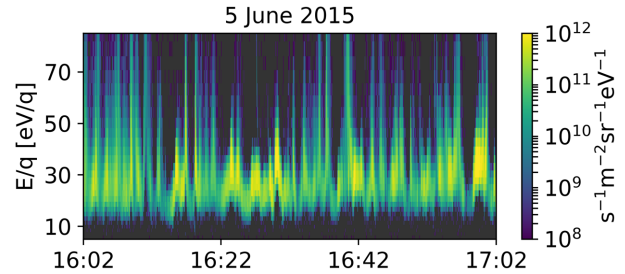


**Figure 5.** An example of an energy–time spectrogram of an hour-long sequence used to classify the 4 s mode observations as different types.

were removed (totally 16 h). A number of cases occurred where the ion environment changed in the middle of a sequence (79 h totally) and, although such cases are scientifically interesting and worthy of further study, they were not considered here as that would lead too far. Data sequences with too little signal or that contained low ion signatures not yet understood (another total of 79 h) were not included. Finally, we ignored times when the low-energy cut-off is not seen, that is, a considerable number of ions are observed even in the lowest energy bin. This happens when the instrument high voltages drift due to low temperatures (as mentioned in Section 2.1.1). After removal of the sequences described above, 1139 h of data (84 per cent of the recorded data with correct binning) remained and was classified as one of five types.

##### 4.2 The types

The assignment of a certain type to a sequence was based entirely on the qualitative appearance in an energy–time spectrogram. No consideration was made regarding, for example, when in the mission the data were recorded or how far from the comet nucleus the spacecraft was at the time. The types were not given beforehand, and neither was the number of types. However, going through the data set several times, it was found that the observed sequences sorted nicely into five categories. Examples of the different types are shown in Fig. 6. Note that the spacecraft potential is negative in most cases, so that ions are accelerated towards the spacecraft. They are therefore observed with a higher energy than they had outside the potential field of the *Rosetta* spacecraft. This is discussed in more detail in the following sections.

In panel (a) (Type 1), we see an ion population that appear narrow in energy, usually observed at energies between 10 and 30 eV/q. There are small changes in flux with time and small changes also in the observed energies, but the overall impression is a constant narrow band in energy–time space.

In Type 2 [panel (b)], the cold low-energy population seen in Type 1 is accompanied with ion fluxes also at higher energies. Typically, ions are seen all the way to the upper energy limit. Frequently, it looks like two distinct populations are present and sometimes there is a clear gap in energy between the populations, as in the latter half of the time interval shown in panel (b).

At times the cold low-energy ion disappears leaving only accelerated ions, which are seen in a wide energy range from approximately 20 eV/q up to the upper limit. Panel (c) displays an example. The lower boundary in energy is less defined than for the previous types. The ion fluxes do not normally vary much with energy, giving a curtain-like appearance in the spectrogram.

The characteristic feature of Type 4 [shown in panel (d)] is repetitive dispersive structures, where the ion energy decreases with time after an initial acceleration. The energy width of the ion population

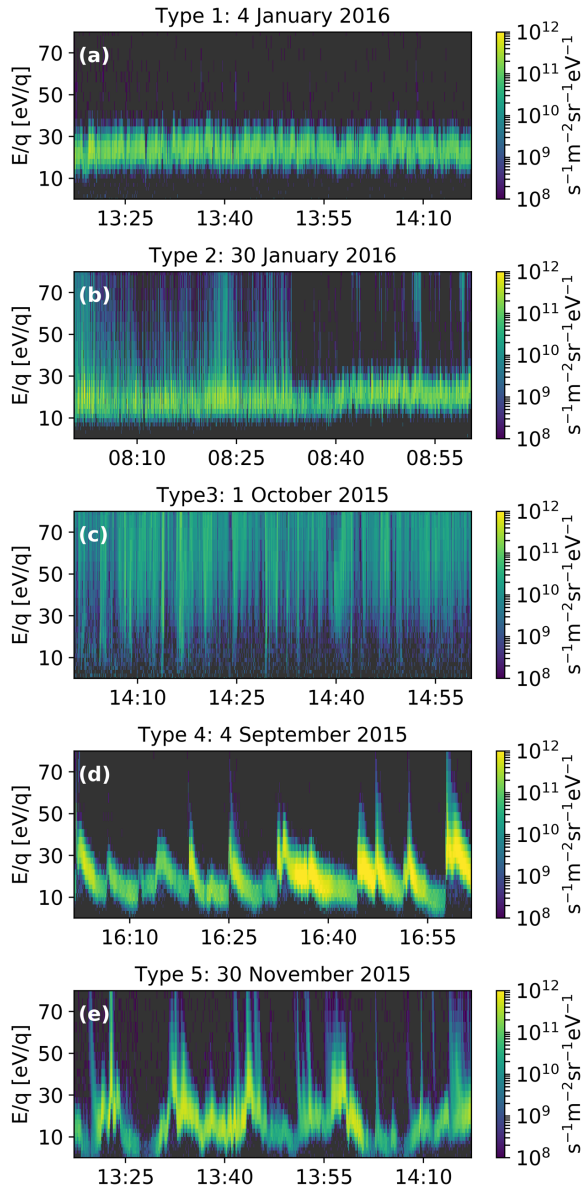


**Figure 6.** Examples of time–energy spectrograms of the five different types of low-energy ion observations.

is almost constant, but the average energy changes significantly. The ion flux also varies with time with a tendency of high fluxes at the same time as the highest average energies.

Finally, the ion population in Type 5, presented in panel (e), is also highly dynamic, with a distinct lower boundary that moves up and down in energy in an irregular pattern. Quasi-periodically, the population gets very wide in energy during a short time. Such ‘spikes’ are often correlated with an increase in differential flux.

### 4.3 When and where

Fig. 7 illustrates when during the mission (that is, how far from the Sun), the different types described in the previous section were observed (upper panel). Each dot corresponds to one hour-long sequence. The leftmost part of the panel is the inbound leg (when the comet was approaching the Sun) and the remaining part shows the outbound leg. Perihelion is marked with  $P$  on the  $x$ -axis.

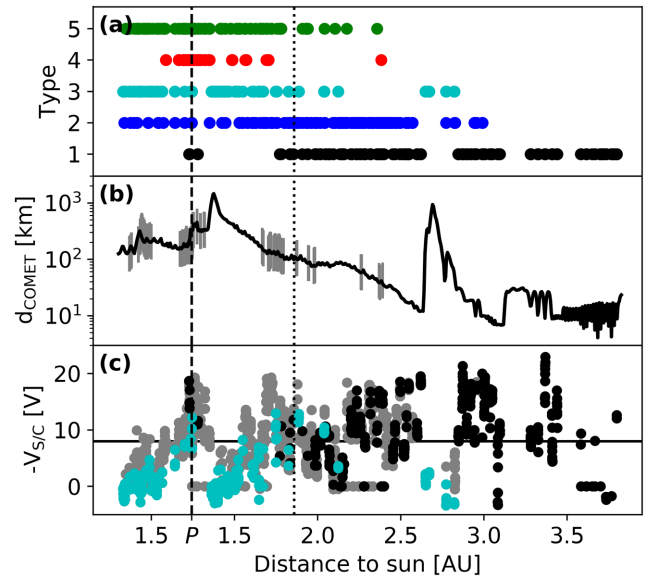


**Figure 7.** (a) The different types and when during the mission they are observed. Each hour-long sequence of data is represented with a coloured dot. The dashed vertical line shows the time of perihelion and the dotted line the return of the solar wind ions in the ion observations. (b) The distance to the comet centre in black (left  $y$ -axis) and the distance to the Sun in red (right  $y$ -axis) versus time. The horizontal black line is arbitrarily put at  $V_{S/C} = -8V$  to guide the eye. The label  $P$  on the  $x$ -axis marks the perihelion distance of 1.24 au. (c) The average value of the negative of the spacecraft potential for all hour-long sequences. Type 1 sequences are shown in black, Type 3 cases in cyan and the remaining types in grey.

The middle panel shows how the distance between *Rosetta* and the comet changes. The observations of the diamagnetic cavity reported in Goetz et al. (2016a) are indicated as vertical lines. More than 660 such observations are made so each individual observation is not visible here. A huge number of diamagnetic cavity detections were made close to perihelion. This is also where most of our Type 4 events were observed. Type 5 events are also only recorded during the time period when the diamagnetic cavity was observed. At distances from the Sun larger than 2.5 au, only Types 1–3 are seen.

The lower panel shows the negative of the average value of the spacecraft potential observed during each hour-long sequence. Values corresponding to Type 1 and Type 3 observations are shown as filled circles in black and cyan, respectively. Spacecraft potential values corresponding to all other types are shown in grey. If the electron temperature does not vary much, the negative of the spacecraft potential is a proxy for the electron density (Odelstad et al. 2015). A more negative potential corresponds to a higher density. We note that Type 3 (cyan) is mostly observed for relatively low electron densities and never really close to the comet (cf. the middle panel). Type 1 events are often (but not always) seen when the density is high. Towards the end of the mission, at large distances from the Sun, all of the data recorded in the 4 s mode belong to this type. The observed electron density was often high as the spacecraft could fly closer to the nucleus than before.

One can imagine a symmetry around perihelion but it is hard to confirm given that high time resolution observations started only in 2015 April–May. In general, the times when the different types are seen are overlapping, showing that other parameters than the location with respect to the Sun and the comet are important. Variations of the solar wind conditions, local plasma instabilities or sudden

**Table 1.** Total observation time of each type of ion dynamics.

Type	Time (h)
1	350
2	337
3	172
4	125
5	155
Wrongly binned	104
Other	219

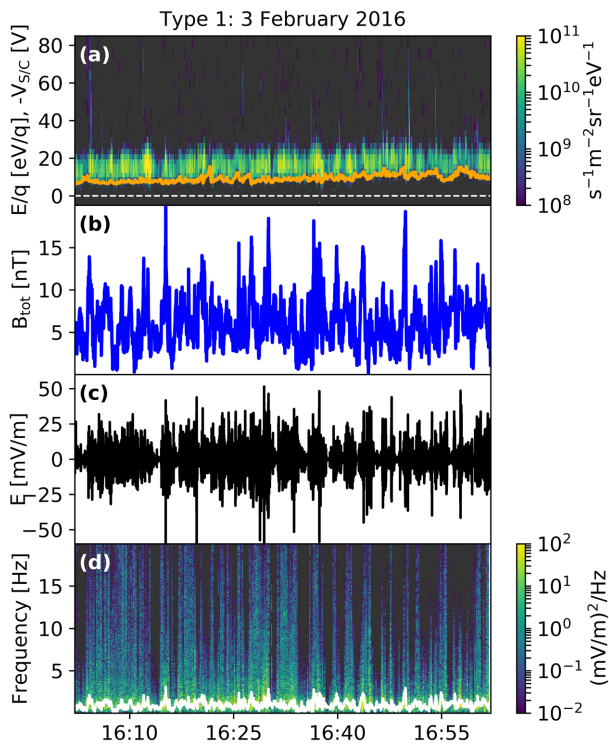


**Figure 8.** Type 1: (a) In colour scale, the observed ion differential flux versus time and energy is shown. The orange line is the negative of the spacecraft potential as observed by RPC-LAP. The dashed white line is put at 0 eV (or V) for reference. (b) The total magnetic field strength versus time. (c) The electric field with the low-frequency component removed. (d) The power spectral density of the electric field versus time and frequency. The white line indicates the estimated lower hybrid frequency.

enhancements of the local neutral density can also influence the ion distributions.

The number of hours respective type was observed is presented in Table 1. However, these values are biased because the observations made with the 4 s mode are not randomly distributed. The fast sampling mode was, for example, more frequently used during the time in the mission when the solar wind ions did not reach the spacecraft (late April 2015 until December 2015; Behar et al. 2017; Nilsson et al. 2017). We present the data here mainly to prove that the types of observations described are not rare cases, but represent typical ion environments in the vicinity of 67P.

#### 4.4 Type 1

Fig. 8 shows an example of Type 1 observations. Here the ion differential flux in panel (a) is plotted together with the negative

of spacecraft potential as observed by RPC-LAP (orange line). The dashed white line is just the zero level, plotted for reference. We see that the lower energy cut-off in the ion data almost perfectly follows the variations of spacecraft potential. The spacecraft potential is obtained from floating probes, and the estimate is likely lower than the true potential as mentioned above (Section 2.3 and Odelstad et al. 2017). Since the spacecraft potential is negative, positive ions are accelerated towards the spacecraft and into the instrument. Ions having an energy of 0 eV outside the potential field of *Rosetta* are measured at an energy corresponding to the spacecraft potential. This must be compensated for in order to find the ‘true’ ion energies and the temperature of the population.

For the hour of data shown here, the median temperature  $kT$  of the distribution is estimated to be 10 eV (7–13 eV), with the range in parentheses representing the 25th and 75th percentiles. The temperature was calculated assuming that the original distribution (outside the potential field of the spacecraft) had no significant drift velocity, but was accelerated by an electrostatic potential towards the instrument. It is also assumed that the effective 2D field of view of RPC-ICA at low energies samples the 3D distribution in a representative way. After removing the energy gain by the electrostatic potential, a Gaussian was fitted to the remaining velocity distribution function for each 4-s-long energy sweep and a histogram of the fit parameter  $kT$  was built. Here one should note that the energy coverage is dense, that is, there are no gaps in energy. The width of each energy bin depends on energy itself and ranges from about 0.5 eV/q (at the lowest energies) to 6 eV/q (at 82 eV/q). Typically, the signal used to estimate the temperature covers five to six energy bins resulting in a well-defined fit. A possible systematic error of the temperature estimate is due to the accuracy of the energy offset correction described in Section 2.1.1. An additional energy offset of  $-1$  eV/q would systematically lower all  $kT$  estimates by about 3 eV. All Type 1 observations made during the mission look similar and the temperature estimate should therefore be representative.

Type 1 dominates the high time resolution observations outside 2.5 au, except during the so-called nightside excursion at the end of 2016 March. With the exception of excursion, when the distance between the comet and the spacecraft increased to almost 1000 km, the spacecraft was close to the comet. The available space for any electric field to accelerate the ions before they arrive at the spacecraft is then limited, which can explain the lack of observations of more accelerated ions at large heliocentric distances. We note that when the distance to the comet increases during the excursion, we observe Type 2 and Type 3 ion distributions instead.

Observations of Type 1 ion distributions are also made closer to the Sun at larger distances from the comet. In these cases, the ion–neutral coupling might play a role. During this period, *Rosetta* is often located close to the distance from the comet where ions and neutrals decouple (Gombosi 2015; Mandt et al. 2016; Vigrén et al. 2017). At times and places where the ion and neutrals are coupled, acceleration may be suppressed and result in Type 1 distributions. If the coupling would be strong, we might expect to observe even colder ions, but recent studies show that even a weak electric field can accelerate ions to a few eV if the ion–neutral coupling is moderate (Vigrén & Eriksson 2017).

The intensity of the ion flux varies on a time-scale of a few minutes and smaller, even faster, variations in flux and energy are seen down to the instrument time resolution of 4 s. In Type 1 events observed at large heliocentric distances towards the end of the mission, there are much less oscillations in flux and energy.

The ions are arriving from almost all directions, and the direction of arrival does not change when the direction of the magnetic field

changes. Directional information is difficult to interpret when the energy of the observed ions is of the same order as the spacecraft potential. The potential field around the spacecraft heavily distorts the particle trajectories (see for example Nyffenegger et al. 2001). Yet, any observed variations in arrival direction should still correspond to variations of the original ion flow direction.

The second panel (b) shows the total magnetic field ( $B_{\text{tot}}$ ). The average field is 6 nT during this period and there are fluctuations with a peak-to-peak amplitude of about 10 nT. In this case, the magnetic field component in the plane perpendicular to the Sun–comet line dominates the magnetic field. The variations in the magnetic field show no obvious correlation to changes in the ion flux or in the spacecraft potential.

From the two Langmuir probes, we can also obtain the electric field in the direction along the probe separation. The procedure is described in Karlsson et al. (2017). Panel (c) in Fig. 8 shows the observed electric field with the low-frequency signal removed by subtracting a running mean. Clearly, fluctuations are present in the electric field during the entire period with a typical amplitude of 25 mV m<sup>-1</sup>. Waves close to the lower hybrid frequency have previously been observed close to 67P (Karlsson et al. 2017). Lower hybrid waves are expected to grow on density gradients and the comet plasma environment seems to favour the generation of them (André et al. 2017). Hence, lower hybrid waves are expected to be common around 67P and also important when discussing ion distributions as they are able to transfer energy between ions and electrons and thereby reshaping the plasma environment (André et al. 2017). Assuming a plasma dominated by singly charged water ions, the fluctuations we observe are in the lower hybrid frequency range, which can be seen from panel (d). Here the power spectral density of the electric field is plotted versus time and frequency. The overplotted white line shows the lower hybrid frequency, computed as  $\frac{1}{2\pi} \sqrt{\omega_{ci}\omega_{ce}}$ , where  $\omega_{ci}$  and  $\omega_{ce}$  are the water ion and the electron gyrofrequency, respectively.

#### 4.5 Type 2

In Type 2 observations, the relatively low-and-narrow-in-energy population is accompanied by a burst-like ion population at higher energies. An example of Type 2 is seen in Fig. 9. As before, panel (a) displays the ion differential flux and as for Type 1, the lower energy boundary correlates to the changes in spacecraft potential, the negative of which is plotted as the orange line. The low-energy part of the ion population looks similarly wide in energy as the Type 1 example shown in the previous section. The low-energy ions also contribute most of the ion flux. Computing the temperature ( $kT$ ) of the distribution the same way as described in the previous section yields 23 eV (18–30 eV).

During a large part of the mission, Types 1 and 2 are alternately seen at the same heliocentric and cometocentric distances. For a time interval close to perihelion, only Type 2 is observed and at the largest distances from the Sun towards the end of the mission only Type 1, as can be seen in Fig. 7.

The energy range of the additional population of accelerated ions varies widely. Sometimes there is a clear gap in energy between the two populations as towards the end of the time interval in Fig. 6(b), while sometimes the higher energy population is connected in energy to the low-energy part, as in our current example (Fig. 9a). On smaller time-scales, it may, however, still look as two distinct populations, see below.

The magnetic field varies with a higher typical amplitude in this case [panel (b)] and the average magnetic field strength is also

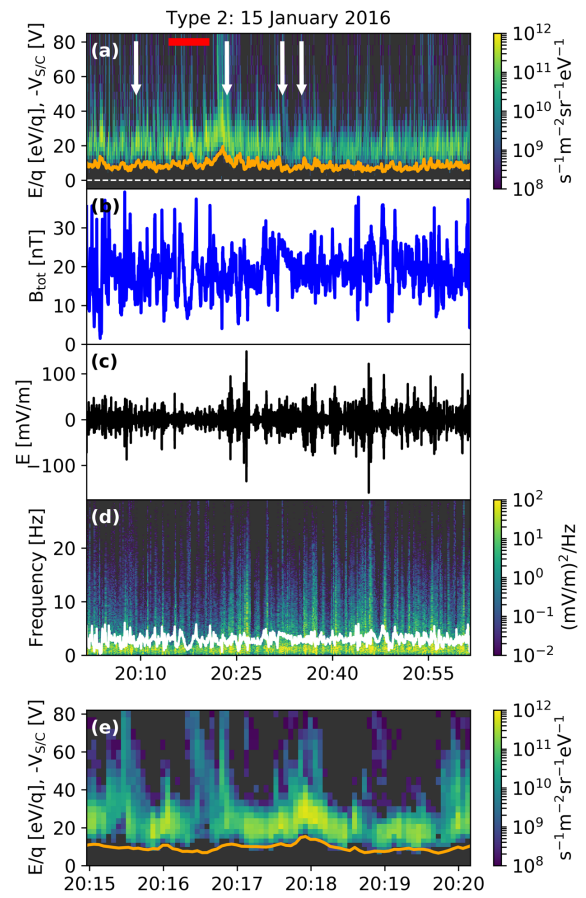


**Figure 9.** Type 2: (a) In colour scale, the observed ion differential flux versus time and energy is shown. The orange line is the negative of the spacecraft potential as observed by RPC-LAP. The dashed white line is put at 0 eV (or V) for reference. (b) The total magnetic field strength versus time. (c) The electric field with the low-frequency component removed. (d) The power spectral density of the electric field versus time and frequency. The white line indicates the estimated lower hybrid frequency. (e) Differential ion fluxes zoomed in on a shorter time interval indicated by the red bar in panel (a).

higher, 18.8 nT. The field component perpendicular to the Sun–comet line dominates the magnetic field strength. The electric field occasionally shows amplitudes of 100 mV m<sup>-1</sup> [panel (c)], but these bursts are not correlated with any particular structure seen in the ion data. The wave frequency is still in the lower hybrid frequency range [panel (d)].

To estimate the time-scales of typical changes in the ion population, we look at a shorter time interval shown in Fig. 9(e). The interval shown is marked with a red bar in Fig. 9(a). We see that the sudden appearances of accelerated ions last for only a few pixels in time, which corresponds to 5–20 s. We also observe a dispersion-like structure starting at 20:16:30 UT, where first ions close to the upper energy limit are seen, followed by ions with lower and lower energies. Dispersive structures in accelerated ions observed on time-scales less than half a minute are a common feature of Type 2 cases. The ion plasma environment is clearly highly variable, suggesting electric and magnetic field variations on small spatial and/or temporal scales.

Finally, we investigate the direction of arrival of the ions. Fig. 10 shows the ion flux recorded in the different azimuthal sectors (corresponding to the different arrival directions in the aperture plane)

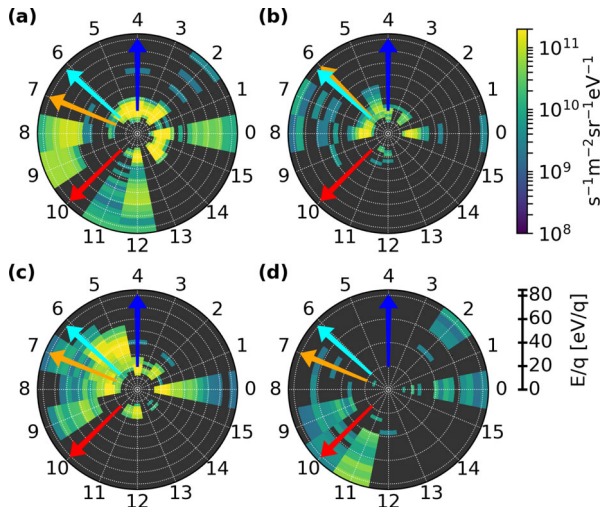


**Figure 10.** Four examples of observed ion fluxes (colour scale) in different directions. The numbers on the circumference correspond to the different sectors and the radial distance from the centre corresponds to energy. The arrows denote the direction towards the Sun (red) and the comet (blue). The orange and cyan arrows are the projections of the total magnetic field and the component of the magnetic field perpendicular to the comet–Sun line.

during four selected energy sweeps. The selected times are marked with white arrows in Fig. 9(a). The radial direction corresponds to energy. The direction towards the Sun and the comet lies almost in the aperture plane, and their respective directions are shown as a red and a blue arrow. The orange and cyan arrows are the projections of the total magnetic field and the component of the magnetic field perpendicular to the comet–Sun line. The low-energy population arrives at the instrument from all directions, although it can vary slightly from energy sweep to energy sweep. Occasionally, the population is not seen at all for one or two sweeps, like in panel (d). The arrival direction of the accelerated ion varies much more and is at a given time normally confined to three to four sectors. Sometimes there are clearly two different populations with different energies like in panel (a), but sometimes such a distinction is not obvious as in panel (c). Sector 0 picks up signal from all other sectors and the signal there should not be trusted.

#### 4.6 Type 3

In Type 3, no low-energy population is seen. One reason for that could be that in many of the Type 3 cases the spacecraft potential is close to zero or even positive, which means ions are repelled from the spacecraft. In such cases, a low-energy ion population still can exist in the plasma but would not be measured. In the case shown in Fig. 11, the average estimated spacecraft potential is still  $-4.6$  V on average, but no low-energy ions are detected. The ions in this case are arriving from a direction in between the direction towards the Sun and the direction to the comet with a rather broad angular distribution (three to four azimuthal sectors, which is about  $90^\circ$ ). The direction stays the same even when the magnetic field direction changes. No temperature estimate is meaningful in this case as RPC-ICA only measures part of the ion population.

This type of ion observation is mainly made at distances larger than  $\approx 100$  km from the comet. For example, such observations were common during the so-called dayside excursion, when *Rosetta* travelled to a cometocentric distance of 1600 km in 2015 October. During the excursion, several fast varying features were seen in the

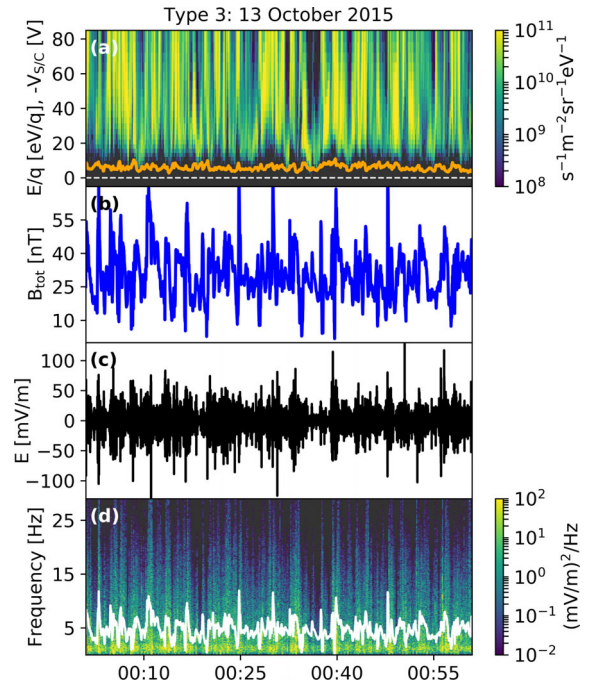


**Figure 11.** Type 3: In colour scale, the observed ion differential flux versus time and energy is shown. The orange line is the negative of the spacecraft potential as observed by RPC-LAP. The dashed white line is put at 0 eV (or V) for reference. (b) The total magnetic field strength versus time. (c) The electric field with the low-frequency component removed. (d) The power spectral density of the electric field versus time and frequency. The white line indicates the estimated lower hybrid frequency.

magnetic field and in Langmuir probe current data, with time-scales of a few seconds to a minute, which were interpreted as magnetic flux ropes passing over the spacecraft (Edberg et al. 2016). Type 3 ion energy spectra were also seen during an observation of mirror mode waves (Volwerk et al. 2016). *Rosetta* was then at more than 200 km distance from the nucleus.

The flux intensity measured in Type 3 cases is often rather constant with energy, but sometimes we see intensity peaks that may move up and down in energy. More common are flux intensity variations as in the example shown. The intensifications in this case are 4–40 s long, which is rather typical.

The magnetic field magnitude is high for this example (about 30 nT), most of which is contributed by the magnetic field component in the plane perpendicular to the Sun–comet line. The fluctuations have an amplitude of 40 nT, peak to peak. The electric field amplitude is also high, generally  $50 \text{ mV m}^{-1}$  with occasional spikes of  $100 \text{ mV m}^{-1}$ , as displayed in panel (c). The wave frequency observed can even in this case be regarded to be in the frequency range of lower hybrid waves [panel (d)].

#### 4.7 Type 4

The dispersive structures characterizing Type 4 are clearly seen in Fig. 12(a): rapid increase of the observed ion energy and a subsequent slower return of the ion energy to the same level as before the sudden increase. The increase occurs within about 20 s, while the ‘relaxation’ takes a couple of minutes. The time between two sudden increases in energy is typically of the order of 1–5 min. The pattern is sometimes this simple but more complex structures can also appear, as at 15:30 UT. Structures with slowly rising energies are

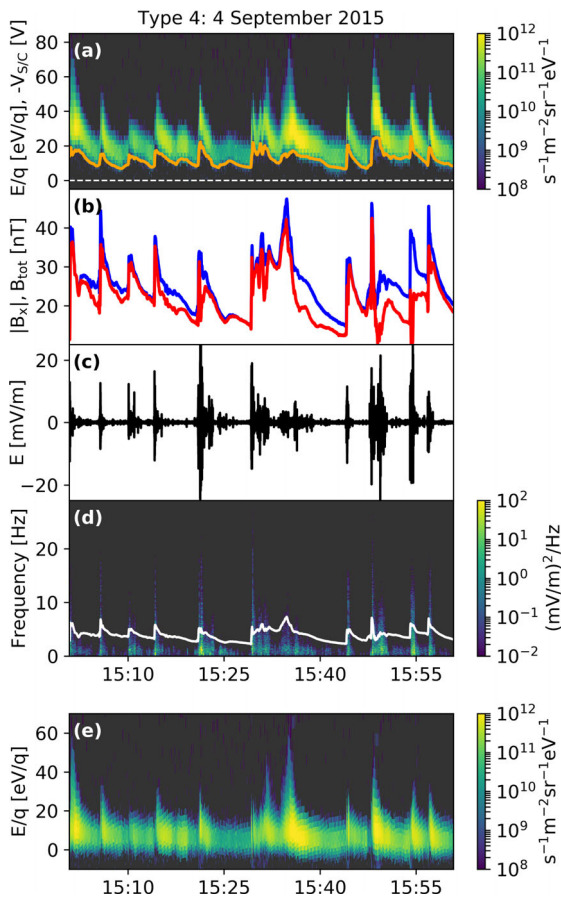


**Figure 12.** Type 4: (a) In colour scale, the observed ion differential flux versus time and energy is shown. The orange line is the negative of the spacecraft potential as observed by RPC-LAP. The dashed white line is put at 0 eV (or V) for reference. (b) The total magnetic field strength versus time (in blue) and the absolute value of the magnetic field component along the comet–Sun line ( $B_{x, \text{CSEQ}}$ ) as a red line. (c) The electric field with the low-frequency component removed. (d) The power spectral density of the electric field versus time and frequency. The white line indicates the estimated lower hybrid frequency. (e) Ion differential flux as in panel (a) but with the energy corrected for the spacecraft potential.

also sometimes seen but are rare. The ion flux intensity also varies, usually reaching a maximum close to where the energy peaks.

The negative of the spacecraft potential [orange line in panel (a)] follows the lower energy ion cut-off, just as for Types 1 and 2, but it is notable how smoothly the spacecraft potential varies here. The previously seen small-scale fast variations are absent here both in the spacecraft potential and in the ion data. The ions are arriving at the instrument from all observable directions, and the temperature of the ion population, following the calculation method outlined in Section 4.4, is  $kT=10$  eV (5–14 eV).

Most of the energy variation seen in the ion data comes from the changes of the spacecraft potential. Compensating for that, assuming that RPC-LAP picks up 85 per cent of the true potential gives the ion spectrogram shown in panel (e). Only very small jumps in energy remain in the ion data.

The magnetic field is likewise smooth. The variation of the field strength (blue line in panel (b)) follows almost exactly the changes in the spacecraft potential and the ion energy. It is the magnetic field component along the Sun–comet line ( $x_{\text{CSEQ}}$ ) that dominates the magnetic field here. This component is plotted as the red curve in

panel (b). The average magnetic field strength during the displayed time interval is 25 nT.

The magnetic field structure is similar to what has been reported just outside the diamagnetic cavity (the field-free region surrounding 67P; Goetz et al. 2016a,b). Type 4 sequences are also the ones that are observed closest to diamagnetic cavities as can be seen from Fig. 7. More than 660 observations of the diamagnetic cavity have been made, and we calculated the time difference between all observed ion sequences (using the time in the middle of respective sequence) to the nearest cavity boundary. For a sequence of Type 4, the median distance in time to a cavity boundary is 12 h, while it is 18 h for a Type 5 sequence. Types 2 and 3 are typically more than 100 h away (178 and 118 h, respectively) from the diamagnetic cavity and Type 1 1600 h. For Types 4 and 5, we can estimate the typical distance to the cavity boundary if we assume that the cavity boundary is spherical and centred on the comet and that the boundary does not move during the time between the ion measurement and the nearest cavity observation. With these assumptions, the median distance to the cavity boundary is 0.40 km for Type 4 and 0.49 km for Type 5. For the other types, the times between cavity boundary and ion observations are too large for these assumptions to be valid.

As explained in Section 4.3, the negative of the spacecraft potential is a proxy for density if the electron temperature is constant. Hence, we conclude that there seem to be semi-regular increases in density (increase in the negative of the spacecraft potential and increase in ion flux) coinciding with increases in magnetic field strength. This may be what characterizes the plasma environment closest to the diamagnetic cavity. Recent observations made by the Mutual Impedance Probe (Trotignon et al. 2007) confirm the tendency for plasma density to increase with magnetic field amplitude in the vicinity of diamagnetic cavities (Henri et al. 2017).

Panel (c) in Fig. 12 shows that the electric field fluctuations are smaller than in the previous cases, with amplitudes just reaching  $20 \text{ mV m}^{-1}$  in a few cases. Also in this case, there is wave activity close to the lower hybrid frequency. The largest wave amplitudes, however, occur just at what appear to be density gradients as well as sharp increases in the magnetic field. In this case, as opposed to the previous, the magnetic and electric fields are both strongly correlated with the ion observations down to time-scales of 20 s. Assuming the plasma convects over the spacecraft with  $0.7 \text{ km s}^{-1}$  that corresponds to a spatial scale of 14 km.

#### 4.8 Type 5

The final type (Type 5) has a couple of similarities with Type 4, which is seen in Fig. 13. The lower energy cut-off often varies significantly together with the spacecraft potential. Most of the ion flux is found in a low-energy population, where dispersive structures similar to those seen in Type 4 still can occur but normally with a faster relaxation. Intermittently, though, ‘spikes’ of accelerated ions are seen with energies reaching the upper limit of the energy range. Compared to Type 2, the changes are smoother and the fast small-scale variations are absent. A typical time between two spikes is a minute or so. The temperature found is  $kT=18$  eV (10–29 eV).

The general appearance of the magnetic field is similar to what was seen for Type 4, but with a higher frequency variation superimposed. The impression is still smoother than for Types 1–3. Most of the magnetic field comes from the Sun–comet line component as in Type 4. The average field strength in this case is 40 nT.

The electric field also shows clear similarities with our previous case. The electric field waves are clearly stronger at the plasma gradients but panel (c) shows amplitudes up to  $100 \text{ mV m}^{-1}$ , which

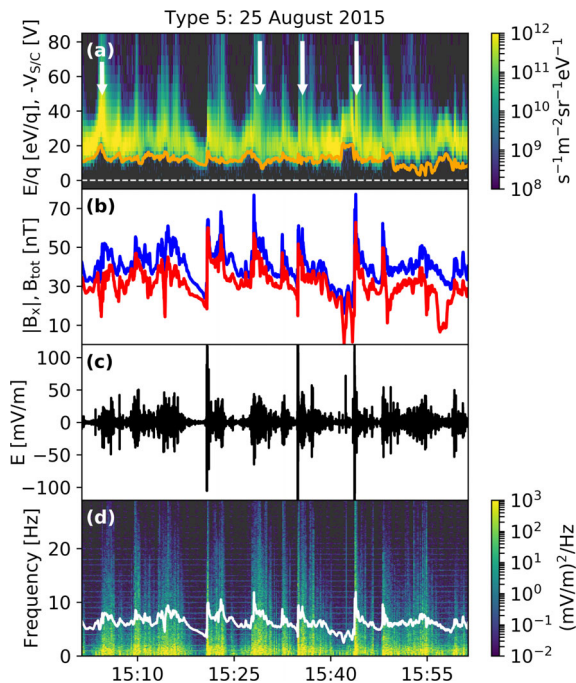


**Figure 13.** Type 5: (a) In colour scale, the observed ion differential flux versus time and energy is shown. The orange line is the negative of the spacecraft potential as observed by RPC-LAP. The dashed white line is put at 0 eV (or V) for reference. (b) The total magnetic field strength versus time. (c) The electric field with the low-frequency component removed. (d) The power spectral density of the electric field versus time and frequency. The white line indicates the estimated lower hybrid frequency.

is much higher than for Type 4. Most of the power spectral density shown in panel (d) is at frequencies just below the estimated lower hybrid frequency. This type of ion spectrum is present in the lower hybrid wave case analysed in André et al. (2017).

Fig. 14 shows the arrival directions of the ions for four selected ‘spikes’. The times of the selected energy sweeps are marked with white arrows in Fig. 13(a). We note that the low-energy ions here seem connected to the high-energy ions in the spikes. Energy sweeps (c) and (d) show a dispersive structure, where the arrival direction changes as the energy increases (sectors 9–11 in panel (c) and 8–10 in panel (d)). Energy–angle dispersion in ion data is further discussed in Nicolaou et al. (2017). The general direction of arrival in sweeps (a) and (c) is from somewhere between the Sun (red arrow) and the comet (blue arrow) direction. The magnetic field has a similar direction projected on to the aperture plane for the four sweeps shown but the ion arrival direction is still changing.

## 5 DISCUSSION

Considering the ever-changing and dynamic environment around 67P, it is remarkable that a majority of all the ion data recorded with the high time resolution mode can be classified as belonging to one of only five types. It suggests that the number of plasma processes and plasma regimes relevant for shaping the ion environment at the cometocentric distances probed are limited. In relation to that, one should also consider that *Rosetta* for a long time, from 2015 April–May until 2015 mid-December, was located in a region void of solar wind ions (Behar et al. 2017; Nilsson et al. 2017). The plasma environment outside and inside of the solar wind cavity boundary may be very different. The dotted line in Fig. 7 shows the return of the solar wind ions in the observations, and, indeed, this seems to

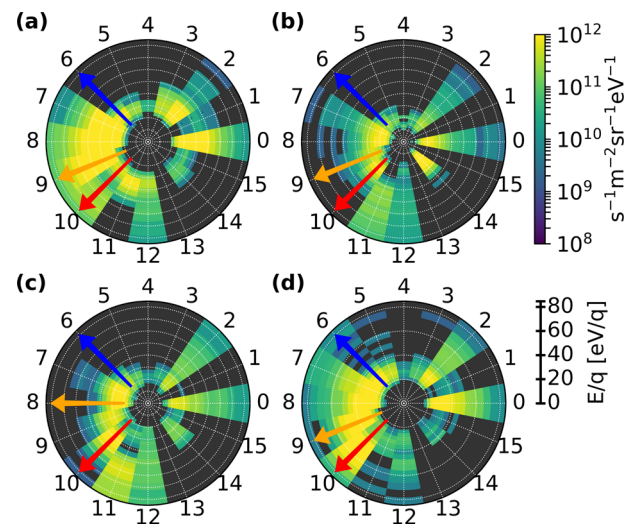


**Figure 14.** Four examples of observed ion fluxes (colour scale) in different directions. The numbers on the circumference correspond to the different sectors, and the radial distance from the centre corresponds to energy. The arrows denote the direction towards the Sun (red) and the comet (blue). The orange arrow is the projection of the total magnetic field on to the aperture plane.

be an important parameter. Type 1 is almost entirely observed after this time, while Types 3, 4 and 5 are mainly observed before.

Type 1 events look very quiet from an ion perspective. There are no large gradients in the ion fluxes or the spacecraft potential and no accelerated ions are observed. Still there is a considerable amount of wave activity seen in the electric field. What is generating these waves? First, it should be noted that we use the spacecraft potential resampled to the ion data, which means there may be density gradients on time-scales shorter than 4 s that could be the source. Secondly, the magnetic field (with 1 s resolution) also shows reasonably large fluctuations from a low average value. Such short-time-scale variations of the magnetic field might correspond to drifts and currents that could lead to instabilities. Finally, we do see small fluctuations in the ion fluxes and in the spacecraft potential. Maybe even these small-scale gradients can cause wave growth.

Our Type 4 case bears large similarities to what is observed outside the diamagnetic cavity. Several authors suggest that the cavity boundary is unstable and most likely affects the surroundings (Goetz et al. 2016b; Henri et al. 2017). The ion structures we observe are perhaps characteristic of such an unstable region around the diamagnetic cavity. The time-scales involved match what we observe. Henri et al. (2017), for example, present rise times of a few tens of seconds for the plasma density around a cavity, with plasma density decay time of a few minutes.

## 6 CONCLUSIONS

In this paper, we have shown how we enabled ion measurements at comet 67P with much higher time resolution than initially planned for. Uploading new lookup tables to the spacecraft allowed RPC-ICA to observe the cometary ion environment with either a 4 s resolution covering the energy range 0.3–82 eV/q or a 1 s resolution covering energies ranging from 13 to 50 eV/q. (The energy ranges here are corrected for the offset.) The 1 s mode was only used at a few occasions, but 1462 h of data were recorded in the 4 s mode from 2015 April until one week prior to the end of mission.

The 4 s data were categorized according to the visual appearance in energy–time spectrograms and five different types of ion

environments were identified. From the characterization of the different types, we conclude the following:

- (1) 84 per cent of the recorded ion data fit the characteristics of one of the five generic types of energy–time spectrogram.
- (2) Variations in ion flux intensity and observed ion energy typically occur on time-scales of 10 s to several minutes.
- (3) Dispersive structures (where the ion energy changes smoothly with time or arrival direction) are common and occur with different time constants (seconds to minutes).
- (4) The low-energy ions (observed up to 40 eV/q) approach the spacecraft from all directions simultaneously.
- (5) The accelerated ions (observed from 40 eV/q to the upper energy limit) can have fast varying flow directions that are not obviously correlated with changes in the magnetic field.

## ACKNOWLEDGEMENTS

The work of GSW is supported by the Swedish National Space Board through grant 96/15. Work at the Royal Belgian Institute for Space Aeronomy was supported by the Belgian Science Policy Office through the Solar-Terrestrial Centre of Excellence and by PRODEX/ROSETTA/ROSINA PEA 4000107705. The RPC-ICA and the RPC-LAP instruments on *Rosetta* are supported by the Swedish National Space Board contracts 95/15 and 101/15. The data used in this paper will soon be made available on the ESA Planetary Science Archive and are available upon request until that time.

## REFERENCES

- Alfvén H., 1957, *Tellus*, 9, 92  
 André M. et al., 2017, *MNRAS*, 469, S29  
 Barnard E. E., 1920, *ApJ*, 51, 102  
 Behar E., Nilsson H., Alho M., Goetz C., Tsurutani B., 2017, *MNRAS*, 469, S396  
 Bieler A. et al., 2015, *A&A*, 583, A7  
 Biermann L., 1951, *Z. Astrophys.*, 29, 274  
 Carr C. et al., 2007, *Space Sci. Rev.*, 128, 629  
 Cravens T., Gombosi T., 2004, *Adv. Space Res.*, 33, 1968  
 Cravens T. E., Kozyra J. U., Nagy A. F., Gombosi T. I., Kurtz M., 1987, *J. Geophys. Res.*, 92, 7341  
 Edberg N. J. T. et al., 2015, *Geophys. Res. Lett.*, 42, 4263  
 Edberg N. J. T. et al., 2016, *MNRAS*, 462, S45  
 Eriksson A. I. et al., 2007, *Space Sci. Rev.*, 128, 729  
 Eriksson A. I. et al., 2017, *A&A*, 605, A15  
 Galand M. et al., 2016, *MNRAS*, 462, S331  
 Glassmeier K.-H., Boehnhardt H., Koschny D., Kührt E., Richter I., 2007a, *Space Sci. Rev.*, 128, 1  
 Glassmeier K.-H. et al., 2007b, *Space Sci. Rev.*, 128, 649  
 Goetz C. et al., 2016a, *A&A*, 588, A24  
 Goetz C. et al., 2016b, *MNRAS*, 462, S459  
 Gombosi T. I., 2015, in Keiling A., Jackman C. M., Delamere P. A., eds, *Physics of Cometary Magnetospheres, in Magnetotails in the Solar System*. Wiley, Hoboken, NJ, p. 169  
 Gunell H. et al., 2017, *A&A*, 600, A3  
 Hansen K. C. et al., 2016, *MNRAS*, 462, S491  
 Hässig M. et al., 2015, *Science*, 347, aaa0276  
 Henri P. et al., 2017, *MNRAS*, 469, S372  
 Johansson F. et al., 2017, *MNRAS*, in press  
 Karlsson T. et al., 2017, *Geophys. Res. Lett.*, 44, 1641  
 Koenders C., Glassmeier K.-H., Richter I., Ranocha H., Motschmann U., 2015, *Planet. Space Sci.*, 105, 101  
 Mandt K. et al., 2016, *MNRAS*, 462, S9  
 Maynard N. C., 1998, in Pfaff R. F., Borovsky J. E., Young D. T., eds, *Electric Field Measurements in Moderate to High Density Space Plasmas With Passive Double Probes, in Measurement Techniques in Space Plasmas Fields*, ch. 2. American Geophysical Union, Washington, DC, p. 13

- Meier P., Glassmeier K.-H., Motschmann U., 2016, *Ann. Geophys.*, 34, 691  
 Mendis D. A., Ip W.-H., 1977, *Space Sci. Rev.*, 20, 145  
 Nicolaou G., Behar E., Nilsson H., Wieser M., Yamauchi M., Berčič L., Wieser G. S., 2017, *MNRAS*, 469, S339  
 Nilsson H. et al., 2007, *Space Sci. Rev.*, 128, 671  
 Nilsson H. et al., 2015, *Science*, 347, aaa0571  
 Nilsson H. et al., 2017, *MNRAS*, 469, S252  
 Nyffenegger O., Mildner M., Wurz P., Altwegg K., Balsiger H., Berthelier J. J., 2001, in Harris R. A., ed., *ESA SP-476: Spacecraft Charging Technology*. ESA, Noordwijk, p. 203  
 Odelstad E. et al., 2015, *Geophys. Res. Lett.*, 42, 10126  
 Odelstad E. et al., 2017, *MNRAS*, in press  
 Richter I. et al., 2015, *Ann. Geophys.*, 33, 1031  
 Sierks H. et al., 2015, *Science*, 347, aaa1044  
 Trotignon J. G. et al., 2007, *Space Sci. Rev.*, 128, 713  
 Vigren E., Eriksson A. I., 2017, *AJ*, 153, 150  
 Vigren E. et al., 2017, *MNRAS*, 469, S142  
 Volwerk M. et al., 2016, *Ann. Geophys.*, 34, 1

## APPENDIX A: ENERGY TABLE

Below is the energy table used for 4 s resolution data. This table already contains the correction of  $-13.7$  eV/q. The negative energies in step 0 to 6 correspond to energy steps where no ions can pass through the ion optics.

**Table A1.** Energy table for the 4 s mode.

Step	$E/q$ (eV/q)	$\Delta E/q$ (eV/q)
0	-8.2	-
1	-7.2	-
2	-6.1	-
3	-5.0	-
4	-3.8	-
5	-2.5	-
6	-1.2	-
7	0.3	0.57
8	1.8	0.66
9	3.4	0.77
10	5.2	0.88
11	7.0	0.99
12	8.9	1.12
13	11.0	1.25
14	13.2	1.39
15	15.6	1.54
16	18.1	1.70
17	20.7	1.87
18	23.6	2.04
19	26.6	2.24
20	29.8	2.44
21	33.2	2.65
22	36.8	2.88
23	40.6	3.13
24	44.7	3.39
25	49.0	3.66
26	53.7	3.95
27	58.6	4.27
28	63.8	4.60
29	69.3	4.95
30	75.3	5.32
31	81.5	5.72

This paper has been typeset from a  $\text{\TeX}/\text{\LaTeX}$  file prepared by the author.